

Refinement for Absolute Pose Regression with Neural Feature Synthesis

Shuai Chen¹ Yash Bhalgat²
 Kejie Li¹ Zirui Wang¹

Xinghui Li¹ Jiawang Bian¹
 Victor Adrian Prisacariu¹

¹Active Vision Lab, University of Oxford
²Visual Geometry Group, University of Oxford

Abstract

Absolute Pose Regression (APR) methods use deep neural networks to directly regress camera poses from RGB images. Despite their advantages in inference speed and simplicity, these methods still fall short of the accuracy achieved by geometry-based techniques. To address this issue, we propose a new model called the Neural Feature Synthesizer (NeFeS). Our approach encodes 3D geometric features during training and renders dense novel view features at test time to refine estimated camera poses from arbitrary APR methods. Unlike previous APR works that require additional unlabeled training data, our method leverages implicit geometric constraints during test time using a robust feature field. To enhance the robustness of our NeFeS network, we introduce a feature fusion module and a progressive training strategy. Our proposed method improves the state-of-the-art single-image APR accuracy by as much as 54.9% on indoor and outdoor benchmark datasets without additional time-consuming unlabeled data training.

1. Introduction

Camera relocalization is a crucial task that allows machines to understand their position and orientation in 3D space. It is an essential prerequisite for applications such as augmented reality, robotics, and autonomous driving, where the accuracy and efficiency of pose estimation is important.

Classical methods for solving this problem rely on geometry-based techniques [4, 5, 6, 26, 39, 41, 42, 43] that require explicit feature correspondence search [15, 16, 24, 40, 52, 53], which is a challenging task in itself. Recent Absolute Pose Regression (APR) methods [19, 20, 21] have been shown to be effective in estimating camera pose from RGB images by using convolutional neural networks. They use direct regression and hence offer advantages such as fast inference speed, low memory requirements, and end-to-end training. However, their accuracy is still lower than that of geometry-based techniques [44, 50].

Recent advances in APR [10, 11, 31, 46, 47, 48], partic-

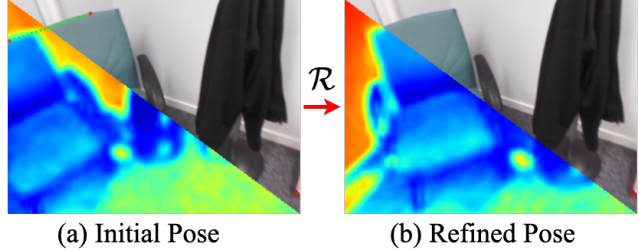


Figure 1: Our pose refinement (R) can improve coarse pose prediction from other methods (a) using novel feature synthesis to find pixel-wise alignment (b) between rendered features (bottom left) and query image (top right).

ularly the use of novel view synthesis (NVS) [10, 11, 27, 30, 31, 48] to generate new images from random viewpoints as data augmentation, have significantly improved the performance. Despite this, state-of-the-art (SOTA) APRs still have the following limitations: i) While the geometry-based methods estimate camera poses by minimizing some cost functions based on multi-view geometry, APR predicts the pose of a query image by passing it through the CNN, which typically disregards geometry in inference time. One of the disadvantages of not taking geometry into account is that the APR network struggles to generalize to viewpoints that the training data fail to cover; ii) The unlabeled data, often sampled from the validation/testing set, used for finetuning the APR network [7, 10, 11] may not be universally available in real-life circumstances, and this semi-supervised finetuning is time-consuming.

To address these limitations, we propose a novel test-time refinement pipeline for APR methods. While traditional geometry-based methods commonly use test-time refinement for improving localization accuracy [9, 26, 41], our post-processing method is the first to integrate a geometric refinement into an end-to-end neural network-based framework. To this end, we design a Neural Feature Synthesizer (NeFeS), which is trained to encode robust 3D geometric features of a scene into an MLP. The NeFeS can render dense feature maps from novel viewpoints for refinement

during testing. To ensure the robustness of the rendered features, we devise a feature fusion module that fuses both color and features, and propose a progressive training strategy for the NeFeS model. Our method leverages the prior literature on volume rendering to inherently constrain geometric consistency during test time using implicit 3D neural feature fields, without relying on an explicit 3D model like most 3D structure-based methods. As such, our approach occupies a middle ground between APR and methods informed by geometry.

We summarize our main contributions as follows: **First**, we propose a test-time refinement pipeline that greatly improves the accuracy of the estimated pose from APR methods without using additional unlabeled data, and produces a new *single-frame* APR SOTA on standard benchmarks. **Second**, we propose a Neural Feature Synthesizer (NeFeS) network that encodes 3D geometric features. Given an initial pose, the NeFeS refines it by rendering a dense feature map, comparing it with the query image features, and back-propagating the error. **Third**, we propose a progressive learning strategy and a feature fusion module to improve the robustness of the rendering ability of the NeFeS model.

2. Related Work

Absolute Pose Regression. In absolute pose regression, the camera pose of an input image is directly regressed using a trained deep network. Several CNN-based backbone architectures have been proposed. PoseNet [19, 20, 21] proposed the first APR solution using GoogLeNet-backbone and has been followed by many different architectures, including the hourglass network [29], attention layers [46, 47, 59], separate layers for predicting the translation and rotation components [33, 61], or LSTM layers [58].

To further improve APR accuracy, some studies propose to utilize sequential information. Most sequential-based APRs utilize temporal constraints such as visual odometry [7, 37, 56], motion [32] or temporal [14] filtering, and multi-tasking [37]. In addition, recent APR methods also obtain significant improvements thanks to advancements in novel view synthesis. One line of approaches focuses on generating a large amount of extra photo-realistic synthetic data [10, 31, 36] using randomly sampled virtual camera poses. Other approaches [10, 11] use NeRF [27, 30] as a direct matching module to perform unlabeled finetuning [7] using extra images without ground-truth pose annotation. The latter approaches, however, usually take tens of hours of extra finetuning time and are based on the assumption that extra unlabeled data can be easily obtained.

Most of the works above focus on means to improve the training of APRs. However, this work focuses on generic APR improvement during the test time. Although other solutions exist for APR’s test-time post-processing, such as those that utilize extended Kalman filter [32], pose graph

optimization [5], or pose auto-encoders [48], our methods can significantly improve arbitrary APR’s performance on both camera positions and orientations and achieve SOTA results without leveraging unlabeled training.

Neural Radiance and Feature Fields. Neural Radiance Fields (NeRF) [30] has attracted many researchers’ interest in recent years and has significantly advanced novel view image synthesis and 3D surface reconstruction. The core of the Neural Radiance Field is an implicit 3D representation and differentiable volume rendering that allow self-supervised optimization from only RGB images without expensive 3D ground-truth annotations. iNeRF [62] firstly shows that NeRF can be inverted to optimize the camera pose. Recent approaches such as NeRF— [60], BARF [25], GARF [13], and NoPe-NeRF [2] show that by treating camera poses as learnable parameters, the NeRF can be simultaneously trained via joint optimization in simple, non-360° scenes. Parallel works such as NICE-SLAM [63] and iMAP [51] use the NeRF representation to predict accurate dense geometry and camera tracking in real-time. Direct-PN [11] uses NeRF as a direct matching module to compute the photometric errors and propagate the error gradients back to the pose regression network. DFNet [10] extends this method to outdoor scenarios by extracting robust features of rendered images using a CNN feature extractor.

Recently, NeRF models have been extended to predict and render *feature fields* in addition to the density and appearance fields. Typically, these feature fields are learned by supervision from a 2D feature extractor using volumetric rendering. [22, 55] showed that these 3D feature fields outperform 2D baselines [8, 23] on downstream tasks such as 2D object retrieval or 3D segmentation. CLIP-Fields [45] showed that the learned feature fields can serve as a scene memory useful for semantic robot navigation. To the best of our knowledge, our work is the first to explore the capability of neural feature fields in camera relocalization task and demonstrate their effectiveness as a test-time pose refinement module.

3. Method

In this section, we present a detailed outline of our approach. Section 3.1 provides a high-level overview of our refinement framework. Section 3.2 describes the architecture and training details of our proposed NeFeS network along with its two components: *Exposure-adaptive Affine Color Transformation (ACT)* and *Feature Fusion module*.

3.1. Refinement Framework for APR

Given a query image I , an absolute pose regression (APR) network, parameterized by a CNN \mathcal{F} in most existing approaches, directly regresses the camera pose \hat{P} of I : $\hat{P} = \mathcal{F}(I)$. The network is typically trained with ground truth image-pose pairs. While APR-based methods

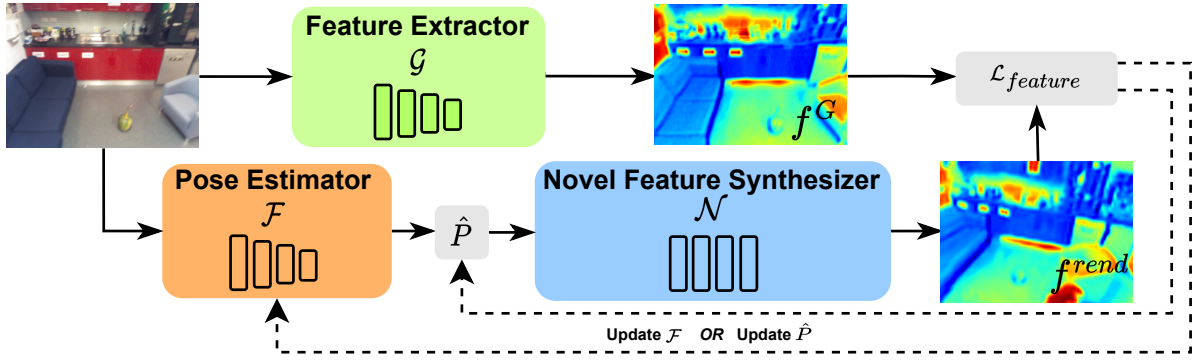


Figure 2: **Illustration of the pose refinement pipeline.** The query image is processed by a pose estimator \mathcal{F} , typically an absolute pose regressor, to obtain a coarse camera pose \hat{P} . Our novel feature synthesizer \mathcal{N} renders a dense feature map f^{rend} based on \hat{P} . Simultaneously, the feature extractor \mathcal{G} extracts the feature map f^G from the query image. We then compute the feature-metric error between f^{rend} and f^G , denoted as $\mathcal{L}_{feature}$. This error is backpropagated to update either the parameters of \mathcal{F} or the coarse pose \hat{P} directly.

are much more efficient than geometry-based methods since they require only a single forward pass of the network, the quality of their predictions is often significantly worse than those of geometry-based methods due to the lack of any 3D geometry-based reasoning [44].

In contrast to much of the prior APR research, which attempts to improve APR by adding constraints to the training loss or making architectural changes to the backbone network, we propose an alternative method to refine the results of APR methods by backpropagating a feature-metric error at inference time. Our method has three major components: (1) a pretrained APR network, denoted as \mathcal{F} , which provides an initial pose; (2) a differentiable novel feature synthesizer \mathcal{N} that directly renders dense feature maps given a camera pose; (3) an off-the-shelf feature extractor \mathcal{G} that extracts the dense feature map of the query image. In our implementation, the feature extraction module from [10] is employed as the feature extractor \mathcal{G} . The refinement procedure is as follows: (i) The query image I is passed through the pretrained APR model \mathcal{F} to predict a coarse camera pose \hat{P} . (ii) The feature synthesizer \mathcal{N} renders a dense feature map $f^{rend} \in \mathbb{R}^{n \times c}$ given the coarse camera pose \hat{P} , where $n = h \times w$, and h and w are the spatial dimensions of the feature map¹. (iii) At the same time, the feature extractor \mathcal{G} extracts a feature map $f^G = \mathcal{G}(I)$ from the query image, where $f^G \in \mathbb{R}^{n \times c}$. (iv) The pose \hat{P} is iteratively refined by minimizing the feature cosine similarity loss $\mathcal{L}_{feature}$ [10] between f^{rend} and f^G :

$$\mathcal{L}_{feature} = \sum_{i=1}^c \left(1 - \frac{\langle f^{rend}_{:,i} \cdot f^G_{:,i} \rangle}{\|f^{rend}_{:,i}\|_2 \cdot \|f^G_{:,i}\|_2} \right) \quad (1)$$

¹Note: We treat the n dimension as the feature rather than c dimension.

where $f^{rend}_{:,i}, f^G_{:,i} \in \mathbb{R}^n$, $\langle \cdot, \cdot \rangle$ denotes the inner product between two vectors and $\|\cdot\|_2$ represents the L2 norm. Different from the common feature matching literatures' [24, 52] convention, our features are normalized along the spatial direction instead of the channel direction to ensure the consistency of the neighboring pixels.

Our method can be regarded as post-processing to the initial pose \hat{P} . We do not save the updated weights of the APR method since we restart from the initial state when given a new query image.

3.2. Neural Feature Synthesizer

We propose a Neural Feature Synthesizer (NeFeS) model that directly renders dense feature maps of a given viewpoint to refine the predictions of an underlying APR network. Similar to NeRF-W [27], our NeFeS architecture uses a base MLP module with *static* and *transient* heads that predict the static and transient density ($\sigma^{(s)}$ and $\sigma^{(t)}$) and view-dependent color ($c^{(s)}$ and $c^{(t)}$) respectively, given an input 3D position (\mathbf{x}) and viewing direction (\mathbf{d}). We use the frequency encoding [30, 57] to encode all 3D positions and view directions. The transient head models the colors of the 3D points using an isotropic normal distribution and predicts a view-dependent variance value (β^2) for the transient color distribution. To render the color of a given pixel, the original volume rendering formulation in NeRF [30] is augmented to include the transient colors and densities, and the color of a given image-pixel ($\hat{\mathbf{C}}(\mathbf{r})$) is computed as a composite of the static and transient components. Here, \mathbf{r} denotes the ray (corresponding to the pixel) on which points are sampled to compute the volume rendering quadrature approximation [28]. The variances of sampled points along the corresponding ray are also rendered using only the tran-

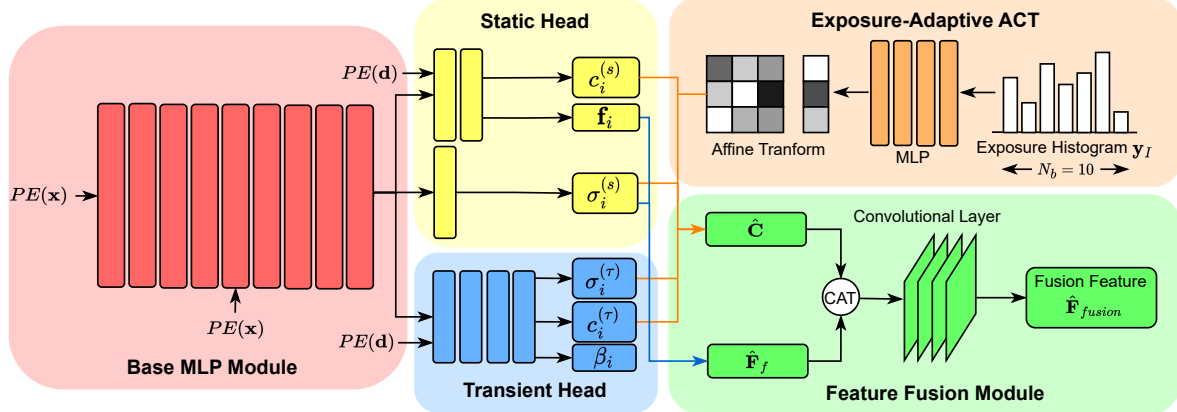


Figure 3: The architecture of our proposed NeFeS model. The query 3D position x is fed to the network after positional encoding $PE(\cdot)$. The network then splits into two heads: the static head and the transient head. Given a viewing direction d , the rendered color map is generated by fusing static RGB value $c_i^{(s)}$, the transient RGB value $c_i^{(\tau)}$ and their corresponding density values $\sigma_i^{(s)}$ and $\sigma_i^{(\tau)}$, while the rendered feature map is formed only by static features f_i and density $\sigma_i^{(s)}$. In addition, the color map adopts exposure-adaptive ACT to compensate for exposure differences between images. The final feature map \hat{F}_{fusion} is the concatenation of rendered RGB and feature map processed by the convolutional fusing layer.

sient densities (and *not* the static densities) to obtain a per-pixel color variance $\beta(r)^2$. We refer the reader to [27] for more mathematical details on the static+transient volume rendering formulation.

We expand the output of the static MLP to also predict features for an input 3D position. The output dimension is $N_c + N_f$, where N_f features are predicted along with RGB values. The per-pixel features are rendered using the same volume rendering quadrature approximation [28]:

$$\hat{F}_f(r) = \sum_{i=1}^N T_i \left(1 - \exp \left(-\sigma_i^{(s)} \delta_i \right) \right) f_i, \quad (2)$$

$$T_i = \exp \left(- \sum_{j=1}^{i-1} \sigma_j^{(s)} \delta_j \right)$$

where f_i and $\sigma_i^{(s)}$ are the feature and density predicted by the static MLP for a sampled point on the ray, and δ_i is the distance between sampled quadrature points i and $i + 1$.

Fig. 3 demonstrates the architecture of our proposed NeFeS model. We propose two crucial components in the rendering pipeline of our NeFeS architecture that ensure robustness of our rendered features.

Exposure-adaptive ACT. In the context of camera relocalization, it is possible that the testing images may have different exposure or lighting conditions than the training sequences. To handle these variations in exposure or lighting, DFNet [10] proposed using the luminance histogram of the query image as a latent code input to the color prediction head of the NeRF MLP. However, since our NeFeS outputs both colors and features at the same time, we find

this approach can perturb the feature output values, causing instability. Ideally, the feature descriptors should be able to maintain locally invariant even under exposure variant circumstances. Inspired by Urban Radiance Fields (URF) [38], we propose to use an *exposure-adaptive Affine Color Transformation (ACT)* which is a 3×3 matrix K plus a 3-dimensional bias vector b predicted using a 4-layer MLP with the query image's luminance histogram y_I as input. Unlike URF, which uses a pre-determined exposure code, we use the query image's histogram embedding to achieve an accurate appearance rendering of the unseen testing images. The final per-pixel color $\hat{C}(r)$ is computed using the affine transformation as $\hat{C}(r) = K\hat{C}_{rend}(r) + b$, where $\hat{C}_{rend}(r)$ is the rendered per-pixel color obtained using the static and transient MLPs.

Feature Fusion Module We propose a Feature Fusion module to fuse the rendered colors and features from the MLPs to produce the final feature map. The rendered colors and features are concatenated and passed into the fusion module consisting of three 3×3 convolution layers followed by a 5×5 convolution layer and a batch normalization layer. During inference, we render the colors and features for all the $H \times W$ image pixels and the resulting $H \times W \times (N_c + N_f)$ tensor is processed by the module. However, during training, for efficiency, we sample $S \times S$ regions to be rendered and apply the loss only to those pixels in each iteration.

We use \mathcal{H} to represent the fusion module. The final output feature result is:

$$\hat{F}_{fusion}(\mathcal{R}) = \mathcal{H}(\hat{C}(\mathcal{R}), \hat{F}_f(\mathcal{R})) \quad (3)$$

where \mathcal{R} is the sampled region as described above.

We experimentally find that the fusion module produces more robust features than the input rendered features $\hat{\mathbf{F}}_f$. We refer readers to Section 4.6 for a detailed ablation study.

3.2.1 Training the Feature Synthesizer

The high-level concept of training the NeFeS network is motivated by the feature field distillation method in [22], which essentially distills the 2D backbone features into a 3D NeRF model. However, the 2D features in our NeFeS need to be closely related to the direct matching formulation [11, 18]. In this work, we use the trained 2D feature extractor from [10] to produce the feature labels due to its effectiveness in generating domain invariant features.

Loss Functions. The total loss used to train our NeFeS model consists of a photometric loss \mathcal{L}_{rgb} and two l_1 -based feature-metric losses:

$$\mathcal{L} = \mathcal{L}_{rgb} + \lambda_1 \mathcal{L}_f + \lambda_2 \mathcal{L}_{fusion}, \quad (4)$$

The photometric loss is defined as the negative log-likelihood of a normal distribution with variance $\beta(\mathbf{r})^2$:

$$\begin{aligned} \mathcal{L}_{rgb}(\mathbf{r}) = & \frac{1}{2\beta_i(\mathbf{r})^2} \left\| \mathbf{C}_i(\mathbf{r}) - \hat{\mathbf{C}}_i(\mathbf{r}) \right\|_2^2 \\ & + \frac{1}{2} \log \beta(\mathbf{r})^2 + \frac{\lambda_s}{K} \sum_{k=1}^K \sigma_k^{(\tau)} \end{aligned} \quad (5)$$

where \mathbf{r} is the ray direction corresponding to an image pixel, $\mathbf{C}_i(\mathbf{r})$ and $\hat{\mathbf{C}}_i(\mathbf{r})$ are the ground-truth and rendered pixel colors. The third term in Eq. (5) is a sum of the transient densities of all the points on ray \mathbf{r} and is used to ensure that transient densities are sparse.

The feature losses are simply l_1 losses:

$$\mathcal{L}_f = \sum_{\mathbf{r} \in \mathcal{R}} \left\| \hat{\mathbf{F}}_f(\mathbf{r}) - \mathbf{F}_{img}(I, \mathbf{r}) \right\|_1. \quad (6)$$

and

$$\mathcal{L}_{fusion} = \sum_{\mathbf{r} \in \mathcal{R}} \left\| \hat{\mathbf{F}}_{fusion}(\mathbf{r}) - \mathbf{F}_{img}(I, \mathbf{r}) \right\|_1. \quad (7)$$

where $\mathbf{F}_{img}(I, \cdot)$ are the features extracted from the training images using the pre-trained 2D feature extractor [10]. Note that, \mathcal{L}_f is applied to the rendered features $\hat{\mathbf{F}}_f$ and \mathcal{L}_{fusion} is applied to the fused features $\hat{\mathbf{F}}_{fusion}$. We experimentally find that using l_1 gives more robust features than l_2 and cosine feature loss for our test time refinement process.

Progressive Training. We propose using a progressive schedule to train the NeFeS model. We first train the color and density part of the network for T_1 epochs to bootstrap the correct 3D geometry for the network. For these epochs, only \mathcal{L}_{rgb} is used. Then we add \mathcal{L}_f with weight λ_1 for the

next T_2 epochs to train the feature part of the static MLP. Since the ground-truth features may not be fully multi-view consistent, we apply *stop-gradients* to the predicted density for the feature rendering branch. And finally, we add the feature fusion loss \mathcal{L}_{fusion} with weight λ_2 for the last T_3 epochs. Since the feature fusion module takes both RGB images and 2D features as input, we randomly sample N_{crop} patches of $S \times S$ regions of the image and features to increase training efficiency. According to our experiments, this progressive training schedule leads to better convergence and performance. In addition, we apply semantic filtering to improve the network training results. Specifically, we use an off-the-shelf panoptic segmentation method [12] to mask out temporal objects in the scene such as people and moving vehicles.

3.3. Direct Pose Refinement

While our method is primarily designed to optimize APR, it is also possible to directly optimize camera pose parameters. We explore this feature by showing a possible scenario wherein the source of the pose estimations is either a black box or cannot be optimized (e.g. the initial camera pose comes from image retrieval). In these settings, we can set up our proposed method to directly refine the camera poses. Specifically, given an estimated camera pose $\hat{P} = [\mathbf{R}|\mathbf{t}]$, where \mathbf{R} is rotation and \mathbf{t} is the translation component, our method optimizes the camera poses using tangent space backpropagation². Additionally, we found that using two different learning rates for the translation and rotation parts helps achieve faster and more stable convergence for camera pose refinement. This is different from the standard convention used in [2, 13, 25, 60]. We refer our readers to supplementary material for more details.

4. Experiments

4.1. Implementation Details

We implement our method in PyTorch [35]. The model is trained with the re-aligned and re-centred poses in SE(3), as in Mildenhall et al. [30]. We use a coarse-to-fine sampling strategy [30] with 64 sampled points per ray in both stages. The width of the MLP layers is 128 and we output $N_c = 3$ and $N_f = 128$ in the last layer of the fine stage MLP. For the exposure-adaptive ACT module, we compute the query image's histogram \mathbf{y}_I in YUV color space and bin the luminance channel into $N_b = 10$ bins. We then feed the binned histogram to 4-layer MLPs with a width of 32. The exposure-adaptive ACT module outputs the exposure compensation matrix \mathbf{K} and the bias \mathbf{b} , which directly transform the integrated colors $\hat{\mathbf{C}}_{NFS}(\mathbf{r})$ of the main networks, with negligible computational overhead. We run the APR refinement process for m iterations per image using the direct

²We use the LieTorch [54] library for this.

Table 1: **Comparisons on Cambridge Landmarks.** We compare our proposed test-time refinement method with single-frame APR methods. The subscript of **NeFeS₅₀** denotes number of optimization iterations used for APR refinement. We report the median position and orientation errors in m/\circ . The best results are highlighted in **bold**.

Methods	Kings	Hospital	Shop	Church	Average
PoseNet(PN) [21]	1.66/4.86	2.62/4.90	1.41/7.18	2.45/7.96	2.04/6.23
PN Learn σ^2 [20]	0.99/1.06	2.17/2.94	1.05/3.97	1.49/3.43	1.43/2.85
geo. PN [20]	0.88/1.04	3.20/3.29	0.88/3.78	1.57/3.32	1.63/2.86
LSTM PN [58]	0.99/3.65	1.51/4.29	1.18/7.44	1.52/6.68	1.30/5.51
MapNet [7]	1.07/1.89	1.94/3.91	1.49/4.22	2.00/4.53	1.63/3.64
TransPoseNet [47]	0.60/2.43	1.45/3.08	0.55/3.49	1.09/4.94	0.91/3.50
MS-Transformer [46]	0.83/1.47	1.81/2.39	0.86/3.07	1.62/3.99	1.28/2.73
[46]+PAE [48]	-	-	-	-	0.96/2.73
DFNet [10]	0.73/2.37	2.00/2.98	0.67/2.21	1.37/4.03	1.19/2.90
DFNet + NeFeS ₅₀ (ours)	0.37/0.62	0.55/0.90	0.14/0.47	0.32/0.99	0.35/0.75

feature matching loss $\mathcal{L}_{feature}$ (cf. Eq. (1)) with a learning rate of 1×10^{-5} . Our default value for m is 50 unless specified, denoted as NeFeS₅₀. The NeFeS model renders features with a shorter side of 60 pixels and then upsample them using bicubic interpolation to 240 for feature matching. Further implementation details about NeFeS, progressive training scheduling, and pose refinement can be found in the supplementary.

4.2. Evaluation on Cambridge Landmarks

We evaluate our proposed refinement method on Cambridge Landmarks [21], which is a popular outdoor dataset used for benchmarking pose regression methods. The dataset contains handheld smartphone images of scenes with large exposure variations and covers an area of $875m^2$ to $5600m^2$. The training sequences contain 200-1500 samples, and test sets are captured from different sequences. For each test image, we refine the model using the approach in Section 3.1 for $m = 50$ iterations.

Table 1 shows summarizes the results of our method and existing APR methods. Our method achieves the state-of-the-art accuracy across all four scenes when coupled with the DFNet [10]. In Section 4.4, we demonstrate the performance of our method with other APR approaches. Particularly, our method can improve by as much as 61.5% compared to prior best scene average results. All the per-scene performances from compared methods are taken from their papers, except for MS-Transformer + PAE [48], which only reports the scene average median errors.

4.3. Evaluation on 7-Scenes

We evaluate our method on Microsoft 7-Scenes dataset [17,49], which includes seven indoor scenes ranging in size from $1m^3$ to $18m^3$ and up to 7000 training images for each scene. We sub-sampled the large training sequences in the dataset to 1000 images for training our NeFeS model. The original ‘ground truth’ (GT) poses are obtained from

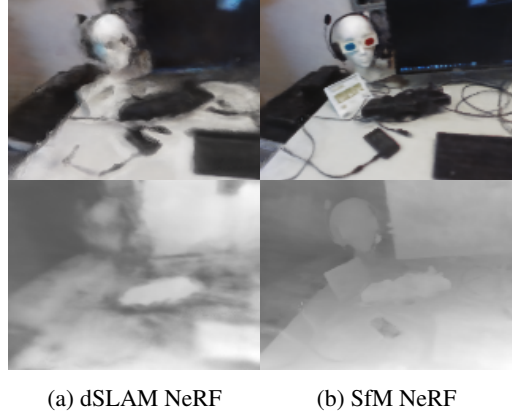


Figure 4: Qualitative comparison between the NeRFs trained by dSLAM GT pose (a) vs. SfM GT pose (b). As illustrated, SfM NeRF (PSNR 19.94 dB) can render superior geometric details (bottom row) than dSLAM NeRF (PSNR 16.11 dB).

RGB-D SLAM (dSLAM) [34]. However, we observe imperfection in the GT poses due to the asynchronous data between the RGB and depth sequences, and this results in low-quality NeRF renderings, as shown in Fig. 4. Thus, we use alternative ‘ground truth’ provided by [3] for our experiments. The authors [3] demonstrate that their camera poses reconstructed by COLMAP, a structure-from-Motion (SfM) library, are more accurate for image-based relocalization. We refer the reader to our supplementary for more details about the GT poses.

For a fair comparison, we use the SfM poses to re-train baseline APR methods using their official code, except for PoseNet, in which we use the open-sourced code from [11]. We trained each APR method 3-4 times to select the best-performing model. We use DFNet + NeFeS₅₀ with the same settings as in Cambridge for our pose refinement experiment. We achieve state-of-the-art results (54.9%+ better in scene average) in all scenes by running 50 optimization steps (see Table 2). The results by using the original ground-truth poses are included in the supplementary, where we also achieve SOTA accuracy.

4.4. Refinement for Different APRs

Table 3 shows the results of our method with different APRs. It shows that our proposed method exhibits versatility, operating beneficially under various APR architectures, such as PoseNet [21], MS-Transformer [46], and DFNet [10]. The pose accuracy is improved with our method in all three APR methods and both datasets.

Table 2: **Comparisons on 7-Scenes dataset.** We compare the proposed refinement method with previous single-frame APR methods. We evaluate all methods with SfM ground truth poses provided in [3], measured in median translational error (m) and rotational error ($^{\circ}$). Numbers in **bold** represent the best performance.

Methods	Chess	Fire	Heads	Office	Pumpkin	Kitchen	Stairs	Average
PoseNet [21]	0.10/4.02	0.27/10.0	0.18/13.0	0.17/5.97	0.19/4.67	0.22/5.91	0.35/10.5	0.21/7.74
MapNet [7]	0.13/4.97	0.33/9.97	0.19/16.7	0.25/9.08	0.28/7.83	0.32/9.62	0.43/11.8	0.28/10.0
MS-Transformer [46]	0.11/6.38	0.23/11.5	0.13/13.0	0.18/8.14	0.17/8.42	0.16/8.92	0.29/10.3	0.18/9.51
PAE [48]	0.13/6.61	0.24/12.0	0.14/13.0	0.19/8.58	0.17/7.28	0.18/8.89	0.30/10.3	0.19/9.52
DFNet [10]	0.03/1.12	0.06/2.30	0.04/2.29	0.06/1.54	0.07/1.92	0.07/1.74	0.12/2.63	0.06/1.93
DFNet + NeFeS ₅₀ (ours)	0.02/0.79	0.02/0.78	0.02/1.36	0.02/0.60	0.02/0.63	0.02/0.62	0.05/1.31	0.02/0.87

Table 3: **Pose refinement on different APR architectures.** Our refinement method can effectively improve pose estimation results for different APR methods. PoseNet is the classic pose regression architecture. MS-Transformer is denoted as MS-Trans., which combines EfficientNet CNN backbones with transformer blocks. DFNet is a multi-task network that predicts domain invariant features and poses.

Dataset	PoseNet	+ Ours	MS-Trans.	+ Ours	DFNet	+ Ours
7-Scenes						
Chess	0.10/4.02	0.04/1.35	0.11/6.38	0.06/1.96	0.03/1.12	0.02/0.79
Fire	0.27/10.0	0.03/1.20	0.23/11.5	0.06/2.55	0.06/2.30	0.02/0.78
Heads	0.18/13.0	0.12/7.91	0.13/13.0	0.09/6.19	0.04/2.29	0.02/1.36
Office	0.17/5.97	0.02/0.72	0.18/8.14	0.05/1.69	0.06/1.54	0.02/0.60
Pumpkin	0.19/4.67	0.06/1.57	0.17/8.42	0.07/1.85	0.07/1.92	0.02/0.63
Kitchen	0.22/5.91	0.02/0.68	0.16/8.92	0.08/2.31	0.07/1.74	0.02/0.62
Stairs	0.35/10.5	0.27/6.35	0.29/10.3	0.34/7.64	0.12/2.63	0.05/1.31
Average	0.21/7.74	0.08/2.83	0.18/9.51	0.11/3.46	0.06/1.93	0.02/0.87
Cambridge						
Kings	1.66/4.86	0.38/0.69	0.83/1.47	0.43/0.59	0.73/2.37	0.37/0.62
Hospital	2.62/4.90	1.15/1.44	1.81/2.39	0.61/1.06	2.00/2.98	0.55/0.90
Shop	1.41/7.18	0.13/0.67	0.86/3.07	0.18/0.98	0.67/2.21	0.14/0.47
Church	2.45/7.96	0.35/1.16	1.62/3.99	0.48/1.53	1.37/4.03	0.32/0.99
Average	2.04/6.23	0.50/0.99	1.28/2.73	0.43/1.04	1.19/2.90	0.35/0.75

Table 4: **Pose refinement on NetVlad** Our method also works on poses initialized with non-APR-based methods, such as NetVlad image retrieval. Since the initial pose error is relatively large, we refine the poses with 100 iterations.

Dataset	NetVlad [1]	Optimize Pose
7-Scenes	0.32/13.72	0.14/3.97
Cambridge	3.18/7.74	1.15/1.30

4.5. Optimize APR vs. Optimize Pose

Besides boosting APR, our proposed approach can also refine the initial coarse camera pose, as outlined in Section 3.3. We first show a use case of this scenario by coupling our method with image retrieval, where the initial pose can only be optimized due to the non-differentiable nature of the retrieval process. Given a query image, we retrieve its nearest neighbor from the training data using NetVLAD [1] and use the associated pose as the initial pose. In this experiment, we set the learning rate to be lr_R and lr_t for rotation

Table 5: **Pose refinement vs. APR refinement** We study on the optimization over APR vs. the pose. Both methods can effectively optimize pose accuracy. However, optimizing APR can obtain lower errors than optimizing poses given the same number of iterations.

Dataset	DFNet	Optimize Pose	Optimize APR
7-Scenes	0.06/1.93	0.04/1.16	0.02/0.87
Cambridge	1.19/2.90	0.66/1.39	0.35/0.75

and translation components, respectively. Specifically, for indoor scenes, we set $lr_R = 0.0087$ (corresponds to 0.5° in radian) and $lr_t = 0.01$. For outdoor scenes, we set $lr_R = 0.01$ and $lr_t = 0.1$. Table 4 summarises the experimental results, indicating substantial improvements in pose accuracy over the NetVLAD retrieved coarse pose, exceeding the performance of many prior APR approaches.

We further conducted a controlled experiment to investigate whether performance disparities exist between two types of optimization: optimizing the APR’s parameters or directly optimizing the pose itself. We evaluated both modes on the DFNet with NeFeS₅₀ refinement, as illustrated in Table 5. The result suggests that while both refinement approaches can effectively improve the pose accuracy, optimizing the neural network’s parameters converges faster than directly optimizing the pose itself. Nevertheless, optimizing the pose remains is also valuable, particularly when the initial pose is derived from a non-differentiable or a black-box pose estimator.

4.6. NeFeS Ablation

This section presents the ablation study of our NeFeS network. In Table 6a, we gradually remove the exposure-adaptive ACT and the Feature Fusion module and evaluate their impact on the performance of our approach on *Cambridge Shop Facade*. The results demonstrate that the removal of each component leads to a deterioration in pose accuracy, indicating the effectiveness of both components. Furthermore, we compare our proposed NeFeS approach with feature maps extracted by a CNN from NeRF-rendered RGB images. Our NeFeS method outperforms the

Table 6: (a) Ablation on NeFeS architecture. (b) Ablation on the proposed training scheduling

(a) NeFeS Architecture Ablation

Method	Shop Facade
NeFeS (ours)	0.14m/0.47°
- Exposure-adaptive ACT	0.14m/1.20°
- Feature Fusion	0.37m/1.62°
NeRF RGB+CNN	0.15m/0.87°

(b) Training Scheduling Ablation

Method	Church
Combined	0.35m/1.13°
Progressive	0.32m/0.99°

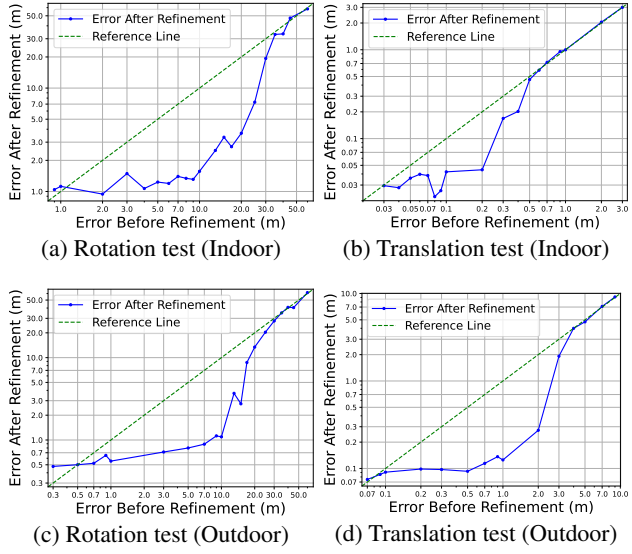


Figure 5: Experiments on pose refinement bounds of our method in indoor and outdoor scenes. Each plot shows errors before (x-axis) and after (y-axis) refinement when ground-truth pose is perturbed by varying magnitudes. Dashed green line is ' $y = x$ '. Points below this line indicate a reduction in pose error using our refinement method.

NeRF+CNN setting in terms of both translational and rotational error, highlighting the effectiveness of our model.

In Table 6b, we compare our progressive training scheduling with the combined scheduling, where all three loss terms have been enabled simultaneously since the beginning of the training. The results reveal that the progressive training scheduling results in better accuracy, providing further support for our design decisions.

4.7. Pose Refinement Bounds

Our proposed refinement method relies on matching rendered features with query image features during test time, so it may fail when there is not sufficient overlap between the two feature maps. To determine the bounds of our refinement method, we randomly perturb the ground-truth pose and determine the maximum perturbation at which our method stops converging. In our experiments, we jitter the orientation or position of the ground truth pose compo-

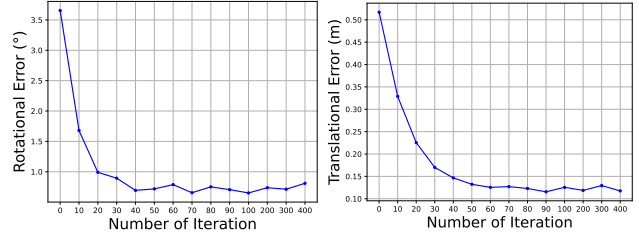


Figure 6: Plots of rotation and translation errors against the number of iteration on *Cambridge: Shop Facade* scene.

nents separately while gradually increasing the magnitude of the perturbation. We use two scenes, an indoor scene (*7-Scenes: Heads*) and an outdoor scene (*Cambridge: Shop Facade*), to illustrate our results in Fig. 5. We observe that our method cannot refine pose errors larger than 35°. In case of translational errors, our method can refine errors upto 0.6m on *Heads* (indoor scene) and upto 4m in *Shop Facade* (outdoor scene). This difference may be caused because of the change in scale between indoor and outdoor settings. For example, in the small-scale scene of *Heads*, the camera is closer to the objects, hence even small movements lead to a large change in the rendering.

4.8. Number of Iterations vs. Accuracy Trade-off

In Fig. 6, we plot the relationship between the number of optimization iterations and pose error. Both translation and rotation errors drop by more than 40% in only 10 iterations. The errors start to plateau around 50 steps. Although we can achieve even lower errors with more iterations, we think this strikes a balance between accuracy and efficiency, and explains how we set our previous experiments.

5. Conclusion

We tackle the camera relocalization problem and improve absolute pose regression (APR) methods by proposing a test-time refinement method. In particular, we design a novel model named Neural Feature Synthesizer (NFS), which can encode 3D geometric features. Given an estimated pose, the NFS renders a dense feature map, compares it with the query image features, and back-propagates the error to refine estimated camera poses from APR methods. In addition, we propose a progressive learning strategy and a feature fusion module to improve the feature robustness of the NFS model. The experiments demonstrate that our method can greatly improve the accuracy of APR methods. Our method provides a promising direction for improving the accuracy of APR methods in real-world applications, where limited resources are often critical factors.

6. Acknowledgments

Shuai Chen was supported by gift funding from Huawei UK. The authors also thank Wenjing Bian, Theo Costain for insightful discussions and proofreading.

References

[1] Relja Arandjelovic, Petr Gronat, Akihiko Torii, Tomas Pajdla, and Josef Sivic. Netvlad: Cnn architecture for weakly supervised place recognition. In *CVPR*, 2016. 7

[2] Wenjing Bian, Zirui Wang, Kejie Li, Jia-Wang Bian, and Victor Adrian Prisacariu. Nope-nerf: Optimising neural radiance field with no pose prior. *arXiv preprint arXiv:2212.07388*, 2022. 2, 5, 13, 15

[3] Eric Brachmann, Martin Humenberger, Carsten Rother, and Torsten Sattler. On the limits of pseudo ground truth in visual camera re-localisation. In *ICCV*, 2021. 6, 7, 12, 13

[4] Eric Brachmann, Alexander Krull, Sebastian Nowozin, Jamie Shotton, Frank Michel, Stefan Gumhold, and Carsten Rother. DSAC - Differentiable RANSAC for Camera Localization. In *CVPR*, 2017. 1, 13

[5] Eric Brachmann and Carsten Rother. Learning Less is More - 6D Camera Localization via 3D Surface Regression. In *CVPR*, 2018. 1, 2

[6] Eric Brachmann and Carsten Rother. Visual camera re-localization from RGB and RGB-D images using DSAC. *arXiv*, 2020. 1, 13

[7] S. Brahmbhatt, J. Gu, K. Kim, J. Hays, and J. Kautz. Geometry-Aware Learning of Maps for Camera Localization. In *CVPR*, 2018. 1, 2, 6, 7, 12, 13

[8] Mathilde Caron, Hugo Touvron, Ishan Misra, Hervé Jégou, Julien Mairal, Piotr Bojanowski, and Armand Joulin. Emerging properties in self-supervised vision transformers. In *Proceedings of the IEEE/CVF international conference on computer vision*, pages 9650–9660, 2021. 2

[9] Tommaso Cavallari, Stuart Golodetz, Nicholas A Lord, Julien Valentin, Luigi Di Stefano, and Philip HS Torr. On-the-fly adaptation of regression forests for online camera re-localisation. In *CVPR*, 2017. 1

[10] Shuai Chen, Xinghui Li, Zirui Wang, and Victor Prisacariu. DFNNet: Enhance absolute pose regression with direct feature matching. In *ECCV*, 2022. 1, 2, 3, 4, 5, 6, 7, 12, 13, 14

[11] Shuai Chen, Zirui Wang, and Victor Prisacariu. Direct-PoseNet: Absolute pose regression with photometric consistency. In *3DV*, 2021. 1, 2, 5, 6, 12, 13

[12] Bowen Cheng, Ishan Misra, Alexander G Schwing, Alexander Kirillov, and Rohit Girdhar. Masked-attention mask transformer for universal image segmentation. In *CVPR*, 2022. 5

[13] Shin-Fang Chng, Sameera Ramasinghe, Jamie Sherrah, and Simon Lucey. Garf: Gaussian activated radiance fields for high fidelity reconstruction and pose estimation. In *ECCV*, 2022. 2, 5, 13, 15

[14] Ronald Clark, Sen Wang, Andrew Markham, Niki Trigoni, and Hongkai Wen. Vidloc: A deep spatio-temporal model for 6-dof video-clip relocalization. In *Proceedings of the IEEE Conference on Computer Vision and Pattern Recognition*, pages 6856–6864, 2017. 2

[15] Daniel DeTone, Tomasz Malisiewicz, and Andrew Rabenovich. Superpoint: Self-supervised interest point detection and description. In *CVPRW*, 2018. 1

[16] Mihai Dusmanu, Ignacio Rocco, Tomas Pajdla, Marc Pollefeys, Josef Sivic, Akihiko Torii, and Torsten Sattler. D2-net: A trainable cnn for joint detection and description of local features. In *CVPR*, 2019. 1

[17] Ben Glocker, Shahram Izadi, Jamie Shotton, and Antonio Criminisi. Real-time rgb-d camera relocalization. In *International Symposium on Mixed and Augmented Reality (ISMAR)*, 2013. 6

[18] M. Irani and P. Anandan. All about direct methods. In *Workshop Vis. Algorithms: Theory Pract.*, 1999. 5

[19] A. Kendall and R. Cipolla. Modelling uncertainty in deep learning for camera relocalization. 2016. 1, 2, 13, 14

[20] A. Kendall and R. Cipolla. Geometric loss functions for camera pose regression with deep learning. In *CVPR*, 2017. 1, 2, 6, 12, 13, 14

[21] A. Kendall, M. Grimes, and R. Cipolla. Posenet: A convolutional network for real-time 6-dof camera relocalization. In *ICCV*, 2015. 1, 2, 6, 7, 12, 13, 14

[22] Sosuke Kobayashi, Eiichi Matsumoto, and Vincent Sitzmann. Decomposing nerf for editing via feature field distillation. In *Advances in Neural Information Processing Systems*, 2022. 2, 5

[23] Boyi Li, Kilian Q Weinberger, Serge Belongie, Vladlen Koltun, and Rene Ranftl. Language-driven semantic segmentation. In *International Conference on Learning Representations*, 2022. 2

[24] Xinghui Li, Kai Han, Shuda Li, and Victor Prisacariu. Dual-resolution correspondence networks. In *NeurIPS*, 2020. 1, 3

[25] Chen-Hsuan Lin, Wei-Chiu Ma, Antonio Torralba, and Simon Lucey. Barf: Bundle-adjusting neural radiance fields. In *ICCV*, 2021. 2, 5, 13, 15

[26] Philipp Lindenberger, Paul-Edouard Sarlin, Viktor Larsson, and Marc Pollefeys. Pixel-Perfect Structure-from-Motion with Featuremetric Refinement. *ICCV*, 2021. 1

[27] Ricardo Martin-Brualla, Noha Radwan, Mehdi S. M. Sajjadi, Jonathan T. Barron, Alexey Dosovitskiy, and Daniel Duckworth. NeRF in the Wild: Neural Radiance Fields for Unconstrained Photo Collections. In *CVPR*, 2021. 1, 2, 3, 4

[28] N. Max. Optical models for direct volume rendering. In *IEEE Transactions on Visualization and Computer Graphics*, 1995. 3, 4

[29] I. Melekhov, J. Ylioinas, J. Kannala, and E. Rahtu. Image-based localization using hourglass networks. In *ICCV Workshops*, 2017. 2, 12, 13

[30] Ben Mildenhall, Pratul P. Srinivasan, Matthew Tancik, Jonathan T. Barron, Ravi Ramamoorthi, and Ren Ng. NeRF Representing scenes as neural radiance fields for view synthesis. In *ECCV*, 2020. 1, 2, 3, 5

[31] Arthur Moreau, Nathan Piasco, Dzmitry Tsishkou, Bogdan Stanciulescu, and Arnaud de La Fortelle. LENS: Localization enhanced by nerf synthesis. In *CoRL*, 2021. 1, 2, 13

[32] Arthur Moreau, Nathan Piasco, Dzmitry Tsishkou, Bogdan Stanciulescu, and Arnaud de La Fortelle. Coordinet: uncertainty-aware pose regressor for reliable vehicle localization. In *Proceedings of the IEEE/CVF Winter Conference on Applications of Computer Vision*, 2022. [2](#), [13](#)

[33] T. Naseer and W. Burgard. Deep regression for monocular camera-based 6-dof global localization in outdoor environments. In *IEEE/RSJ International Conference on Intelligent Robots and Systems (IROS)*, 2017. [2](#)

[34] R. Newcombe, A. Davison, S. Izadi, P. Kohli, O. Hilliges, J. Shotton, D. Molyneaux, S. Hodges, D. Kim, and A. Fitzgibbon. Kinectfusion: Real-time dense surface mapping and tracking. In *In International Symposium on Mixed and Augmented Reality (ISMAR)*, 2011. [6](#), [12](#)

[35] Adam Paszke, Sam Gross, Francisco Massa, Adam Lerer, James Bradbury, Gregory Chanan, Trevor Killeen, Zeming Lin, Natalia Gimelshein, Luca Antiga, et al. Pytorch: An imperative style, high-performance deep learning library. *Advances in neural information processing systems*, 32, 2019. [5](#)

[36] Pulak Purkait, Cheng Zhao, and Christopher Zach. Synthetic view generation for absolute pose regression and image synthesis. In *BMVC*, 2018. [2](#)

[37] N. Radwan, A. Valada, and W. Burgard. Vlocnet++: Deep multitask learning for semantic visual localization and odometry. In *IEEE Robotics and Automation Letters*, 2018. [2](#)

[38] Konstantinos Rematas, Andrew Liu, Pratul P Srinivasan, Jonathan T Barron, Andrea Tagliasacchi, Thomas Funkhouser, and Vittorio Ferrari. Urban radiance fields. In *CVPR*, 2022. [4](#)

[39] Paul-Edouard Sarlin, Cesar Cadena, Roland Siegwart, and Marcin Dymczyk. From coarse to fine: Robust hierarchical localization at large scale. In *CVPR*, 2019. [1](#)

[40] Paul-Edouard Sarlin, Daniel DeTone, Tomasz Malisiewicz, and Andrew Rabinovich. SuperGlue: Learning feature matching with graph neural networks. In *CVPR*, 2020. [1](#)

[41] Paul-Edouard Sarlin, Ajaykumar Unagar, Måns Larsson, Hugo Germain, Carl Toft, Viktor Larsson, Marc Pollefeys, Vincent Lepetit, Lars Hammarstrand, Fredrik Kahl, and Torsten Sattler. Back to the Feature: Learning robust camera localization from pixels to pose. In *CVPR*, 2021. [1](#), [13](#)

[42] T. Sattler, B. Leibe, and L. Kobbelt. Improving image-based localization by active correspondence search. In *European conference on computer vision*, 2012. [1](#), [13](#)

[43] T. Sattler, B. Leibe, and L. Kobbelt. Efficient & Effective Prioritized Matching for Large-Scale Image-Based Localization. In *IEEE TPAMI*, 2017. [1](#), [13](#)

[44] T. Sattler, Q. Zhou, M. Pollefeys, and L. Leal-Taixe. Understanding the limitations of cnn-based absolute camera pose regression. In *CVPR*, 2019. [1](#), [3](#)

[45] Nur Muhammad Mahi Shafullah, Chris Paxton, Lerrel Pinto, Soumith Chintala, and Arthur Szlam. Clip-fields: Weakly supervised semantic fields for robotic memory. In *Workshop on Language and Robotics at CoRL 2022*. [2](#)

[46] Yoli Shavit, Ron Ferens, and Yosi Keller. Learning multi-scene absolute pose regression with transformers. In *ICCV*, 2021. [1](#), [2](#), [6](#), [7](#), [12](#), [13](#), [14](#)

[47] Yoli Shavit, Ron Ferens, and Yosi Keller. Paying attention to activation maps in camera pose regression. In *arXiv preprint arXiv:2103.11477*, 2021. [1](#), [2](#), [6](#), [12](#), [13](#)

[48] Yoli Shavit and Yosi Keller. Camera pose auto-encoders for improving pose regression. In *ECCV*, 2022. [1](#), [2](#), [6](#), [7](#), [12](#), [13](#)

[49] Jamie Shotton, Ben Glocker, Christopher Zach, Shahram Izadi, Antonio Criminisi, and Andrew Fitzgibbon. Scene coordinate regression forests for camera relocalization in rgb-d images. In *CVPR*, 2013. [6](#), [12](#)

[50] Y. Shvit and R. Ferens. Introduction to camera pose estimation with deep learning. *arXiv preprint arXiv: 1907.05272*, 2019. [1](#)

[51] Edgar Sucar, Shikun Liu, Joseph Ortiz, and Andrew Davison. iMAP: Implicit mapping and positioning in real-time. In *Proceedings of the International Conference on Computer Vision (ICCV)*, 2021. [2](#)

[52] Jiaming Sun, Zehong Shen, Yuang Wang, Hujun Bao, and Xiaowei Zhou. LoFTR: Detector-free local feature matching with transformers. *CVPR*, 2021. [1](#), [3](#)

[53] Hajime Taira, Masatoshi Okutomi, Torsten Sattler, Mircea Cimpoi, Marc Pollefeys, Josef Sivic, Tomas Pajdla, , and Akihiko Torii. InLoc: Indoor Visual Localization with Dense Matching and View Synthesis. *CVPR*, 2018. [1](#)

[54] Zachary Teed and Jia Deng. Tangent space backpropagation for 3d transformation groups. In *CVPR*, 2021. [5](#)

[55] Vadim Tschernezki, Iro Laina, Diane Larlus, and Andrea Vedaldi. Neural Feature Fusion Fields: 3D distillation of self-supervised 2D image representations. In *Proceedings of the International Conference on 3D Vision (3DV)*, 2022. [2](#)

[56] A. Valada, N. Radwan, and W. Burgard. Deep auxiliary learning for visual localization and odometry. In *ICRA*, 2018. [2](#), [13](#)

[57] Ashish Vaswani, Noam Shazeer, Niki Parmar, Jakob Uszkoreit, Llion Jones, Aidan N Gomez, Łukasz Kaiser, and Illia Polosukhin. Attention is all you need. *NeurIPS*, 2017. [3](#)

[58] F. Walch, C. Hazirbas, L. Leal-Taixe, T. Sattler, S. Hilsenbeck, and D. Cremers. Image-based localization using lstms for structured feature correlation. In *ICCV*, 2017. [2](#), [6](#), [12](#), [13](#)

[59] Bing Wang, Changhao Chen, Chris Xiaoxuan Lu, Peijun Zhao, Niki Trigoni, and Andrew Markham. Atloc: Attention guided camera localization. In *Proceedings of the AAAI Conference on Artificial Intelligence*, volume 34, pages 10393–10401, 2020. [2](#)

[60] Zirui Wang, Shangzhe Wu, Weidi Xie, Min Chen, and Victor Adrian Prisacariu. NeRF—: Neural radiance fields without known camera parameters. *arXiv preprint arXiv:2102.07064*, 2021. [2](#), [5](#), [13](#), [15](#)

[61] J. Wu, L. Ma, and X. Hu. Delving Deeper into Convolutional Neural Networks for Camera Relocalization. In *ICRA*, 2017. [2](#), [12](#), [13](#)

[62] Lin Yen-Chen, Pete Florence, Jonathan T. Barron, Alberto Rodriguez, Phillip Isola, and Tsung-Yi Lin. inerf: Inverting neural radiance fields for pose estimation. In *arxiv arXiv:2012.05877*, 2020. [2](#), [13](#), [15](#)

[63] Zihan Zhu, Songyou Peng, Viktor Larsson, Weiwei Xu, Hujun Bao, Zhaopeng Cui, Martin R. Oswald, and Marc Pollefeys. Nice-slam: Neural implicit scalable encoding for slam.

In *Proceedings of the IEEE/CVF Conference on Computer Vision and Pattern Recognition (CVPR)*, June 2022. [2](#)

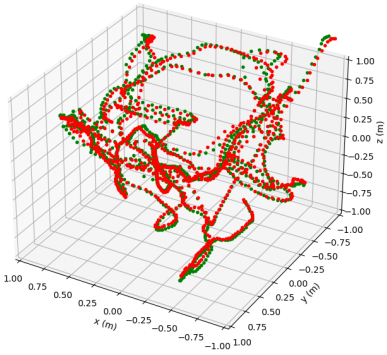


Figure 7: A visualization of camera trajectories of 7-Scene: Chess scene. The original ‘GT’ poses are obtained using dSLAM [34] (green). In this paper, we use SfM GT poses provided by [3] (red) for better GT pose accuracy. Two GT trajectories have a median ATE error of 3.5cm/1.46°.

7. Implementation Details

Here, we provide more implementation details in addition to the ones mentioned in Sec. 4.1 of the main paper.

Progressive training schedule. The training process for the NeFeS network starts with the photometric loss only for $T_1 = 600$ epochs by setting $\lambda_1 = \lambda_2 = 0$ in Eq. (4). The color and density components of the model are trained with a learning rate of 5×10^{-4} which is exponentially decayed to 8×10^{-5} over 600 epochs. We randomly sample 1536 rays per image and use a batch size of 4. After 600 epochs, we reset the learning rate to 5×10^{-4} and switch on the feature loss (\mathcal{L}_f in Eq. (6)) for the next $T_2 = 200$ epochs with $\lambda_1 = 0.04, \lambda_2 = 0$. The fusion loss (\mathcal{L}_{fusion} in Eq. (7)) is switched on for the last $T_3 = 400$ epochs with coefficients $\lambda_1 = 0.02, \lambda_2 = 0.02$. During the third training stage T_3 , instead of randomly sampling image rays, we randomly sample $N_{crop} = 7$ image patches of size $S \times S$ where $S = 16$. To extract image features (i.e. $\mathbf{F}_{img}(I, \cdot)$) as pseudo-groundtruth, we use the finest-level features from DFNet’s [10] feature extractor module. We resize the shorter sides of the feature labels to 60.

8. 7-Scenes Dataset Details

In Sec. 4.3 of the main paper, we mention the difference between the dSLAM-generated ground-truth pose and the SfM-generated ground-truth pose for the 7-Scenes dataset. We provide more details in this section.

dSLAM vs. SfM GT pose Brachmann *et al.* [3] discovered imperfections in the original ‘ground-truth’ poses generated by dSLAM in the 7-Scenes dataset. They used SfM to regenerate a new set of ‘ground-truth’ poses, and re-aligned and re-scaled it to match with dSLAM poses.

Table 7: We compare the proposed refinement method using 7-Scene dSLAM GT pose [49] with prior single-frame APR methods, in average of median translation error (m) and rotation error (°). Numbers in **bold** represent the best performance.

Methods	Average
PoseNet(PN) [21]	0.44/10.4
PN Learn σ^2 [20]	0.24/7.87
geo. PN [20]	0.23/8.12
LSTM PN [58]	0.31/9.85
Hourglass PN [29]	0.23/9.53
BranchNet [61]	0.29/8.30
MapNet [7]	0.21/7.77
Direct-PN [11]	0.20/7.26
TransPoseNet [47]	0.18/7.78
MS-Transformer [46]	0.18/7.28
[46]+PAE [48]	0.15/7.28
DFNet [10]	0.12/3.71
DFNet + NeFeS₅₀ (dSLAM)	0.08/2.83

As described in Sec. 4.3 of the main paper, we notice that when trained with the SfM ground-truth poses, the rendering quality of NeRF is noticeably boosted compared with using the SLAM ground-truth poses. The comparison between the trajectories of two sets of ground-truth pose is visualized in Fig. 7. An interesting observation is made based on the results presented in Table 2 of our main paper. We note that DFNet is able to achieve superior performance when SfM GT is used, compared to its performance reported in the original paper [10]. This phenomenon may be attributed to utilizing the improved synthetic dataset generated by NeRF during DFNet’s *Random View Synthesis* [10] training.

APR Comparisons with dSLAM GT. To supplement the Table 2 in the main paper, we provide the comparison between previous methods and our method when trained and evaluated using dSLAM ground-truth pose. Please refer Table 7 for the results. As shown, our method can also improve the state-of-the-art APR performance by a large margin using dSLAM GT.

9. Comparison to Sequential APR and 3D Approaches

Our method is a single-frame APR method. In Table 8, we compare with geometry-based methods and sequential-based methods for camera localization. The results on 7-Scenes dataset are evaluated using the original SLAM ground-truth pose, except methods marked by ‘COLMAP’ which indicates the results evaluated using the COLMAP ground-truth pose for 7-Scenes. For the first time, we show

Table 8: This table compares different types of camera relocalization on Cambridge Landmarks and 7-Scenes dataset. We show representative methods for each school of approaches: geometry-based methods (3D), sequential-based APR methods (Seq. APR), and single frame APR methods (1-frame APR). We report the average of median median translation error (m) and rotation error ($^{\circ}$). Numbers in **bold** represent the performance of our methods.

Family	Method	Cambridge	7-Scenes
3D	AS [42]	0.29/0.6	0.05/2.5
	AS [43]	0.11/0.3	0.04/1.2
	DSAC [4]	0.32/0.8	0.20/6.3
	DSAC* [6]	0.15/0.4	0.03/1.4
	DSAC* [3, 6] (COLMAP)	0.15/0.4	0.01/0.34
	PixLoc [41]	0.11/0.3	0.03/1.1
Seq. APR	MapNet+PGO [7]	-	0.18/6.55
	CoordiNet [32]	0.92/2.58	0.22/9.7
	CoordiNet+LENS [31]	0.39/1.15	0.08/3.0
	VLocNet [56]	0.78/2.82	0.05/3.80
1-frame APR	PoseNet(PN) [21]	2.04/6.23	0.44/10.4
	PN Learn σ^2 [20]	1.43/2.85	0.24/7.87
	geo. PN [20]	1.63/2.86	0.23/8.12
	LSTM PN [58]	1.30/5.51	0.31/9.85
	Hourglass PN [29]	-	0.23/9.53
	BranchNet [61]	-	0.29/8.30
	MapNet [7]	1.63/3.64	0.21/7.77
	Direct-PN [11]	-	0.20/7.26
	TransPoseNet [47]	0.91/3.50	0.18/7.78
	MS-Transformer [46]	1.28/2.73	0.18/7.28
	[46]+PAE [48]	0.96/2.73	0.15/7.28
	DFNet [10]	1.19/2.90	0.12/3.71
	DFNet + NeFeS₅₀	0.35/0.75	0.08/2.83
	DFNet + NeFeS₅₀ (COLMAP)	0.35/0.75	0.02/0.87

that a single-frame APR method can obtain accuracy in the same magnitude as 3D geometry-based approaches. We also show that when compared with sequential-based APR methods, our method achieves competitive results on Cambridge dataset and 7-Scenes dataset.

10. Comparisons with Photometric Refinement Methods

In this section, we study the differences between featuremetric refinement and photometric refinement. Prior literature such as iNeRF [62], NeRF— [60], BARF [25], GARF [13], and NoPe-NeRF [2], have attempted to ‘invert’ a NeRF model with photometric loss for pose optimization.

However, directly comparing our featuremetric method with these methods would not be appropriate due to the following reasons: **Firstly**, these methods [2, 13, 25, 60] optimize both camera and NeRF model parameters simultaneously but are unsuitable for complex scenes with large motion (e.g. 360°scenes) since each frame’s camera pose is initialized from an identity matrix. **Secondly**, these meth-

Table 9: We compare our featuremetric refinement method using the proposed **NeFeS** network with photometric-based refinement baselines on *Cambridge Hospital*.

Methods	Hospital
DFNet	2.00m/2.98°
DFNet + Sparse NeRF photometric ₅₀	1.19m/1.52°
DFNet + Dense NeRF photometric ₅₀	0.80m/1.12°
DFNet + NeFeS₅₀	0.55m/0.90°

ods do not effectively handle exposure variations, resulting in suboptimal rendering quality. **Thirdly**, even with a coarse camera pose initialization, photometric-based inversion methods cannot prevent drifting in refined camera poses, leading to misalignment with the ground truth poses of testing sequences.

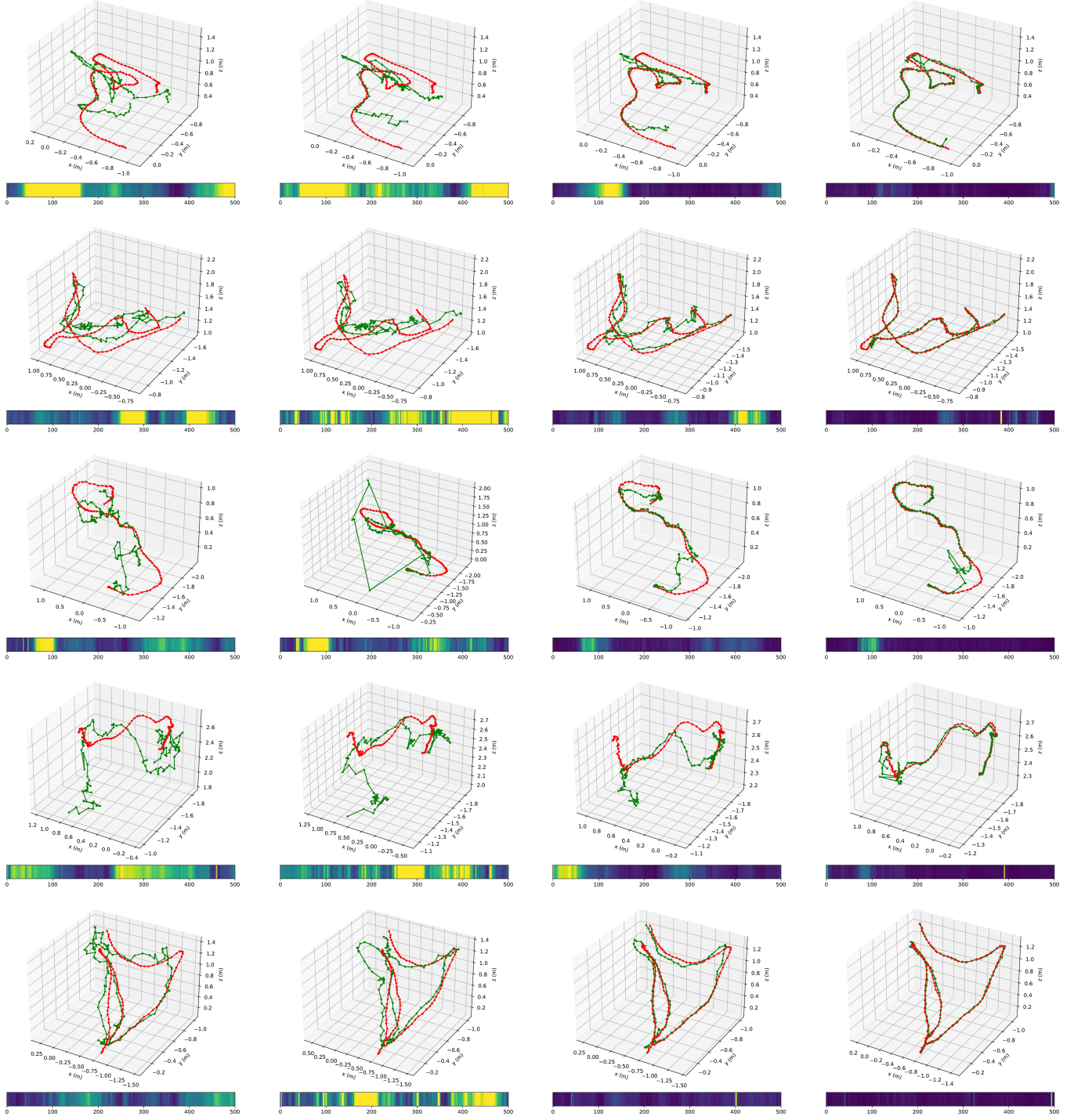
Therefore, for a fair comparison with photometric methods, we define a photometric refinement model as the baseline model to compare with. Specifically, for the baseline model, the main architecture from the NeFeS model is maintained but without the feature outputs, and only the RGB colors $\hat{C}(\mathbf{r})$ are used for photometric pose refinement. The performance of two cases with photometric refinement are demonstrated in Table 9: first is a sparse photometric refinement that randomly samples pixel-rays, similar to iNeRF [62] or BARF [25]-like methods; and the other uses dense photometric refinement, which renders entire RGB images. The results indicate that our featuremetric refinement is more robust than all the photometric refinement baselines, as it achieves lower pose errors after 50 iterations of optimization.

11. Qualitative Comparisons

In Fig. 8, we qualitatively compare the refinement accuracy of different APR methods - namely PoseNet [19, 20, 21], MS-Transformer [46], DFNet [10] - with our method, i.e. DFNet+NeFeS₅₀. We can observe that our method produces the most accurate poses (compared to ground-truth) and has a significant improvement over DFNet in different scenes such as fire [1000-1500] and kitchen [1000-1500].

12. Benefit of splitting lr_R and lr_t

As described in Sec. 3.3 of the main paper, we find using different learning rates for translation and rotation components as beneficial for fast convergence when we directly refine the camera pose parameters. In this section, we use a toy experiment to illustrate how we determine to use this strategy. We select 20% of *Cambridge: Shop Facade*’s test images and perform direct pose refinement for 20 iterations using our NeFeS model. In Table 10, we compare our *different* learning rate setting with several cases of *same* learning



(a) PoseNet [19, 20, 21]

(b) MS-Transformer [46]

(c) DFNet [10]

(d) DFNet+NeFeS₅₀

Figure 8: Qualitative comparison on the 7-Scenes dataset. The 3D plots show the camera positions: **green** for ground truth and **red** for predictions. The bottom color bar represents rotational errors for each subplot, where yellow means large error and blue means small error for each test sequence. Sequence names from top to bottom are: fire [1000-1500], office [2500-3000], pumpkin [500-1000], kitchen [1000-1500], kitchen [1500-2000]. Since each scene has different numbers of frame, we select 500 frames from each of them and append the range after scene’s name.

Table 10: We use a toy example to show the benefit of using *different* learning rates over *same* learning rates for translation and rotation components during direct pose refinement. We show four cases for *same* learning rate including two settings that are used in prior works. Our pose refinement results are evaluated by using 20% test data of *Cambridge: Shop Facade* and 20 iterations of optimization.

LR Settings		Shop-20% (+NeFeS ₂₀)
same lr	Initial Pose Error	0.58m/3.14°
	$lr_R = lr_t = 0.1$	0.91m/22.70°
	$lr_R = lr_t = 0.01$	0.49m/1.51°
	$lr_R = lr_t = 0.003$ [13, 25]	0.54m/2.44°
	$lr_R = lr_t = 0.001$ [2, 60, 62]	0.57m/2.48°
different lr	$lr_R = 0.01, lr_t = 0.1$	0.27m/1.77°

rate settings. We show that by utilizing a different learning rate strategy, the pose error converges much faster and is more stable for both camera position and orientation.